Zitierweise: *Angew. Chem. Int. Ed.* **2023**, *62*, e202309869
doi.org/10.1002/anie.202309869

DNA Nanotechnology | Hot Paper

Minimalist Design of Wireframe DNA Nanotubes: Tunable Geometry, Size, Chirality, and Dynamics

*Xin Luo[+], Daniel Saliba[+], Tianxiao Yang, Serena Gentile, Keita Mori, Patricia Islas, Trishalina Das, Neda Bagheri, Alessandro Porchetta, Alba Guarne, Gonzalo Cosa, and Hanadi F. Sleiman**

Abstract: DNA nanotubes (NTs) have attracted extensive interest as artificial cytoskeletons for biomedical, synthetic biology, and materials applications. Here, we report the modular design and assembly of a minimalist yet robust DNA wireframe nanotube with tunable cross-sectional geometry, cavity size, chirality, and length, while using only four DNA strands. We introduce an h-motif structure incorporating double-crossover (DX) tile-like DNA edges to achieve structural rigidity and provide efficient self-assembly of h-motif-based DNA nanotube (**H-NT**) units, thus producing programmable, micrometer-long nanotubes. We demonstrate control of the **H-NT** nanotube length via short DNA modulators. Finally, we use an enzyme, RNase H, to take these structures out of equilibrium and trigger nanotube assembly at a physiologically relevant temperature, underlining future cellular applications. The minimalist **H-NTs** can assemble at near-physiological salt conditions and will serve as an easily synthesized, DNA-economical modular template for biosensors, plasmonics, or other functional materials and as cost-efficient drug-delivery vehicles for biomedical applications.

Introduction

DNA nanotubes (NTs) are an emerging class of one-dimensional biomaterials with remarkable complexity, structural programmability, and nanometer-scale precision.[1–3] Strategies have been developed to construct nanotube structures with controlled circumference, geometry, length, and rigidity.[1,4–5] Numerous applications have resulted, including cargo delivery vehicles,[6–8] synthetic cytoskeletons,[9–10] membrane channels and molecular transport systems,[11–13] templates for cellular growth and nanoscale organization.[14–17] DNA tile-based nanotubes are typically formed by assembling short bundles of DNA helices for size-defined nanotubes or by wrapping two-dimensional (2D) tile lattices with repeating DNA sequences for extended tubular structures.[18–24] Tiles comprised of a few DNA strands are frequently used as the modular building blocks for these extended structures, enabling dynamic control over the assembly and disassembly through strand displacement and enzymatic processes.[25–32] However, this method only offers rough control of the nanotube circumference and geometry by the inter-tile angles.[1,24] A DNA-brick-based nanotube with a circular cross-section and controlled circumference was assembled, and its size was progressively increased by using four to twenty constituent strands.[33]

In contrast, the DNA origami method permits complete rational design and precise regulation of nanotube length, circumference, and shape, with the challenge of requiring hundreds of distinct DNA sequences to assemble these structures.[34–37] Although the length of each origami tube is constrained by the size of the origami scaffold, longer nanotubes can be created hierarchically.[38–39]

Tile-based, brick-based and DNA origami nanotubes are composed of densely packed DNA helices, which impart rigidity to the structures but generally require high-salt buffer solutions (e.g., Mg^{2+}) for stable assembly. This limits their ability to function in biologically relevant conditions with low salt concentrations.[40–41] Conversely, our laboratory has reported the construction of wireframe DNA nanotubes with excellent stability in low-salt conditions due to their reduced inter-helix electrostatic repulsion.[5–6,42–43] These nanotubes are produced by stacking "rung" units of well-defined geometries onto one another and linking them using DNA double-strands.[44–45] However, due to the relatively short persistence length of double-stranded DNA and the

[*] X. Luo,[+] D. Saliba,[+] K. Mori, P. Islas, T. Das, G. Cosa, H. F. Sleiman
Department of Chemistry, McGill University
801 Sherbrooke St. West, Montreal QC, H3A 0B8 (Canada)
E-mail: hanadi.sleiman@mcgill.ca

T. Yang, A. Guarne
Department of Biochemistry and Centre de Recherche en Biologie Structurale, McGill University
Montreal QC (Canada)

S. Gentile, N. Bagheri, A. Porchetta
Department of Chemistry, University of Rome Tor Vergata, Rome (Italy)

[+] These authors contributed equally to this work.

nicks in the structure, DNA-duplex-edged wireframe structures are more flexible and susceptible to structural distortions.[42,46] Double-crossover (DX) motifs, consisting of two adjacent DNA helices, demonstrate greater persistence length than double-stranded DNA (dsDNA).[47–51] However, their use as structure edges has been limited to discrete cage structures and wireframe DNA origami.[49,52–53]

Here, we report a minimalist design of a robust h-motif-based DNA nanotube (**H-NT**). Our **H-NT** design, assembled with only four DNA components, provides full control over the nanotube's geometry, circumference, and chiral twist, unlike other examples of DNA-minimal NTs. A new h-motif structure is designed to assemble around a core strand into rung units with rigid DX-tile-like edges (Figure 1), which then polymerize into nanotubes. The rung monomer geometry can be tuned from triangular to square to pentagonal by simply changing one of its four strands. The rigidity of the h-motif-based nanotube is demonstrated by molecular dynamics (MD) simulations and experimentally micron-scale nanotubes formed through a simple one-pot annealing approach. A unique feature of our **H-NT** is that the twist of the NT can be easily tuned by changing a few DNA bases in the design while maintaining the same number of DNA components. So far, only DNA-intensive methods like DNA origami have demonstrated the ability to precisely control structural chirality and global twist. Our design is the first to demonstrate chirality/twist control in DNA minimal structures, which will serve as a tunable, cost-effective material to construct chiral plasmonic structures, sensors, and structures that exhibit circularly polarized luminescence. We demonstrate that DNA invader strands of different lengths provide a facile and modular method to tune the nanotube length and dispersity. Interestingly, an RNA invader and RNase H enzyme can change the nanotube assembly mechanism to produce nanotubes at physiologically relevant temperatures. The minimalist design of these nanotubes and their synthesis from only four strands is especially advantageous for biological applications that often require a significant

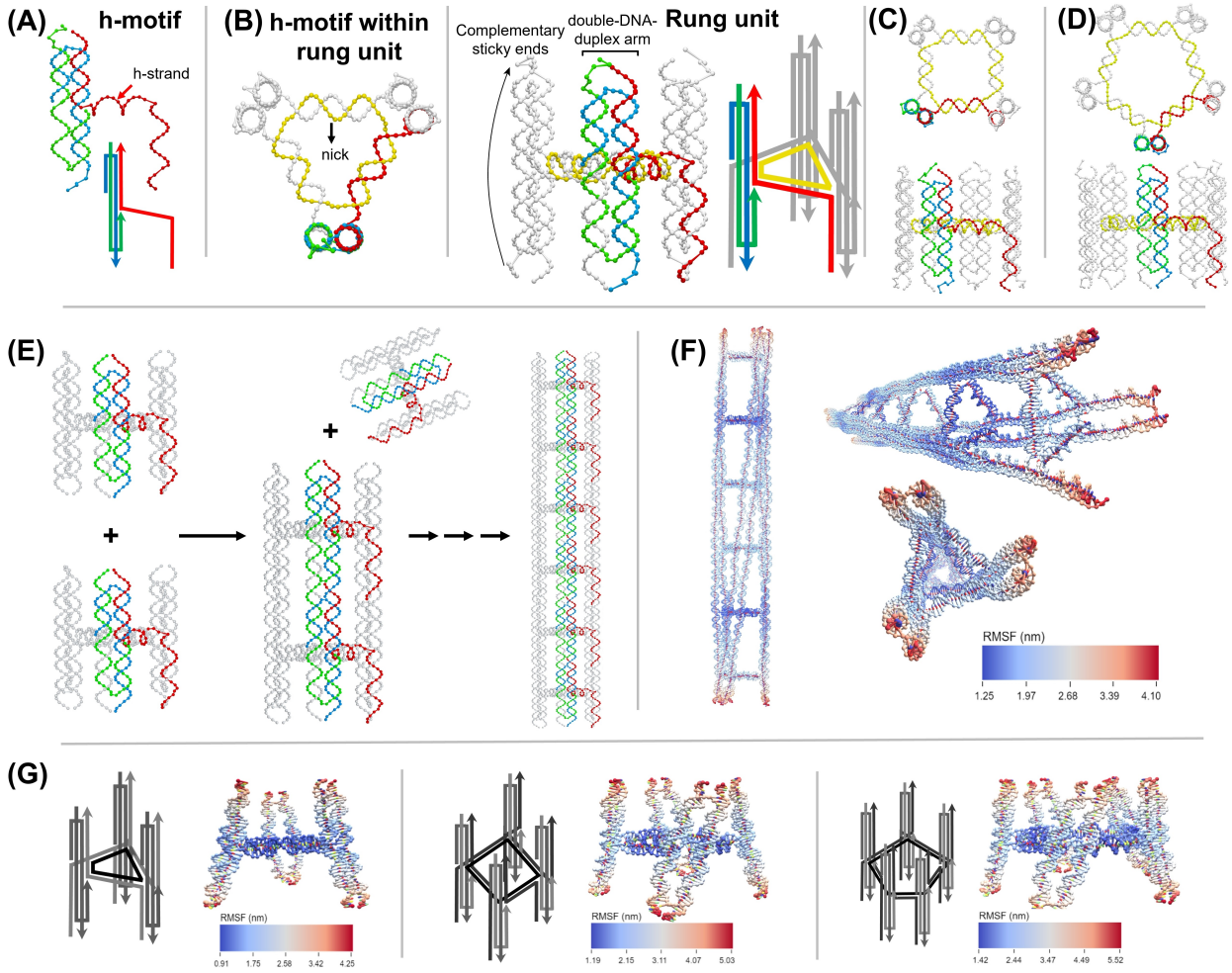

Figure 1. **H-NTs** designs and MD simulated mean structures. (A) The h-motif is composed of three sequences: two interlocked arm strands, T1 and T2 (green and blue) and the h-strand (red). Designs of the (B) triangular, (C) square, and (D) pentagonal **H-NT** rung units, each consisting of the same h-motif and a central strand (yellow) with repeating sequence and increasing length. (E) **H-NT** formation by stacking triangular rungs through sticky end hybridization. While a stepwise mechanism is shown here for clarity, nanotube assembly occurs upon one-pot annealing of the four component strands. (F) Mean configuration and root-mean-square fluctuations (RMSF) of a triangular **H-NT** hexamer from MD simulation. (G) Schematic illustration and MD simulated mean configuration of triangular, square, and pentagonal rungs (left to right).

amount of material and costly chemical modifications of DNA to prevent enzymatic degradation.[2,54–55] These rigid modular nanotubes with controllable cavity sizes and lengths are stable and can be assembled in low salt concentrations relevant to physiological conditions, rendering them promising candidates for multivalent biosensing scaffolds and drug-delivery vehicles for biomedical applications.

Results and Discussion

To achieve a robust wireframe DNA nanotube structure while using a minimum number of DNA strand components, we developed an h-motif, which includes two anti-parallel DNA duplexes arranged side by side (Figure 1A). Like a DX tile structure, we propose that two adjacent connected DNA duplexes can impart additional rigidity to structure edges. As shown in Figure 1A, an h-motif is made from three DNA sequences and consists of a double-DNA-duplex arm with two inter-locked strands, T1 (green) and T2 (blue), and an "h-strand" (red) crossing from the arm to the central C3 strand (yellow) and then to the next h-motif (Figure 1B). Hence, a triangular **H-NT** rung can be created by hybridizing three identical h-motifs to the central DNA strand with three-fold rotational symmetry (see movie 1). The central strand of the triangular rung comprises three repeating sequences at each edge once folded into a circular conformation during assembly, allowing three identical h-motifs to bind. Using the same h-motif, rungs with square (Figure 1C), pentagonal (Figure 1D), and potentially larger cross-sectional geometries can also be produced by merely extending the core strand with four, five, or more sequence repeats, respectively. By modifying a single sequence, this adaptable method provides a simple way to adjust the nanotube cavity volume for potential cargo encapsulation or selective encapsulation of nanoparticles of various sizes.[6,43] Each h-motif arm has two complementary 5-nucleotide sticky ends at its two termini. Triangular, square, and pentagonal rungs (Figure 1G), therefore, have six, eight, and ten sticky ends, respectively, at one end that are complementary to corresponding sticky ends at the other end. Therefore, extended nanotubes can assemble by stacking rungs via hybridization of their sticky ends (Figure 1E).

With MD simulation tools,[56–57] we first investigated the structural robustness of **H-NTs** assembled using triangular rungs. As depicted in Figure 1F, the mean configuration resulting from the MD simulation revealed well-aligned rungs in a straight linear arrangement with no notable bending or distortion. Additional simulation results on **H-NT** with various cross-section geometries suggested triangular **H-NT** as a particularly rigid structure (Figure 1G and Figure S4). Our previous single-DNA-duplex wireframe nanotubes often faced the problem of backbone bending and distortion, resulting in limited 1D structure formation and collapsed tube cavities (Figure S1). To confirm the rigidity of the h-motif-based nanotube backbone, the sticky-ends of two arms in the triangular rung were deleted before the MD simulation, leaving rungs aligned by only one h-motif backbone. As shown in Figure S3, NT rungs were evenly aligned on one side of the backbone with no zig-zag distortions. On the other hand, our previous single-DNA-duplex nanotubes showed significant deviation from longitudinal alignment (Figure S1).

To experimentally verify the **H-NT** design, we performed a one-pot thermal annealing assembly of its four constituent strands. Micrometer-long tubular structures were observed by AFM (Figure 2A–C). By changing the core strand from one containing three-repeat sequences to ones containing four- or five-repeats, triangular (Figure 2A), square (Figure 2B), and pentagonal (Figure 2C) nanotubes were formed, respectively. The rungs of **H-NT** can be clearly observed in the AFM images. For example, in Figure 2D, the height profile along a square **H-NT** axis presents periodic features of 2.0–2.3 nm (red arrows), which correspond to the rung centers. From the height profile, the average distance between rungs is 14.5–14.8 nm, which is consistent with the rung length ($\approx$14.3 nm) from the design (42 nucleotides, 0.34 nm/nucleotide) and MD simulations (Figure 2E). Cryo-electron microscopy (cryo-EM) confirmed the long tubular structures of **H-NTs** and clearly showed their rung-stacking topologies, with marked differences between the three cross-sectional geometries in their near-native states (Figure 2F–H, and Figure S13). Cryo-EM images showed an increase in the nanotube's width from 10 nm to 13 nm to 15 nm for a triangular, square, and pentagonal cross-sectional geometry, respectively, whereas the distance between two consecutive rungs is 14.2–14.4 nm, which is consistent with those obtained by AFM and MD simulations, with a nanotube width increase from 9 nm to 14 nm to 15 nm, respectively.

Notably, due to the wireframe design and multivalent sticky end hybridization, **H-NTs** can assemble in as low as 2.5 mM Mg^{2+} buffer (Figure S31), which is close to the Mg^{2+} concentration in physiological conditions.[58] This property renders **H-NTs** excellent candidates in biological applications, such as modular delivery vehicles and multivalent biosensor scaffolds.

Total internal reflection fluorescence (TIRF) was additionally employed to determine the native state of **H-NTs** in solution (see movies 2 and 3).[59] To accomplish their fluorescence imaging, a Cy3 modification was introduced at the 5′ end of the central strand, and the fluorescently labeled **H-NT** was placed between two glass slides separated by 320 nm. This arrangement confines the motion of large nanotubes to roughly two dimensions. The average contour length of tubular structures longer than 500 nm measured from the fluorescence images for **H-NTs** having triangular (Figure 3A) and pentagonal (Figure 3B) geometries was found to be 1.38 ± 0.72 μm and 2.65 ± 0.38 μm, respectively (Figure S49). The length of 500 nm was chosen as the analysis threshold to exclude two diffraction-limited **H-NTs** randomly located next to each other. The increase in length between the triangular and pentagonal nanotubes is consistent with the increased stability provided by the greater number of sticky ends connecting two consecutive rungs.

In the MD simulations of the **H-NT** structure, we observed a slight global bending of the backbone and a twist of the rungs along the nanotube axis, which manifested as a

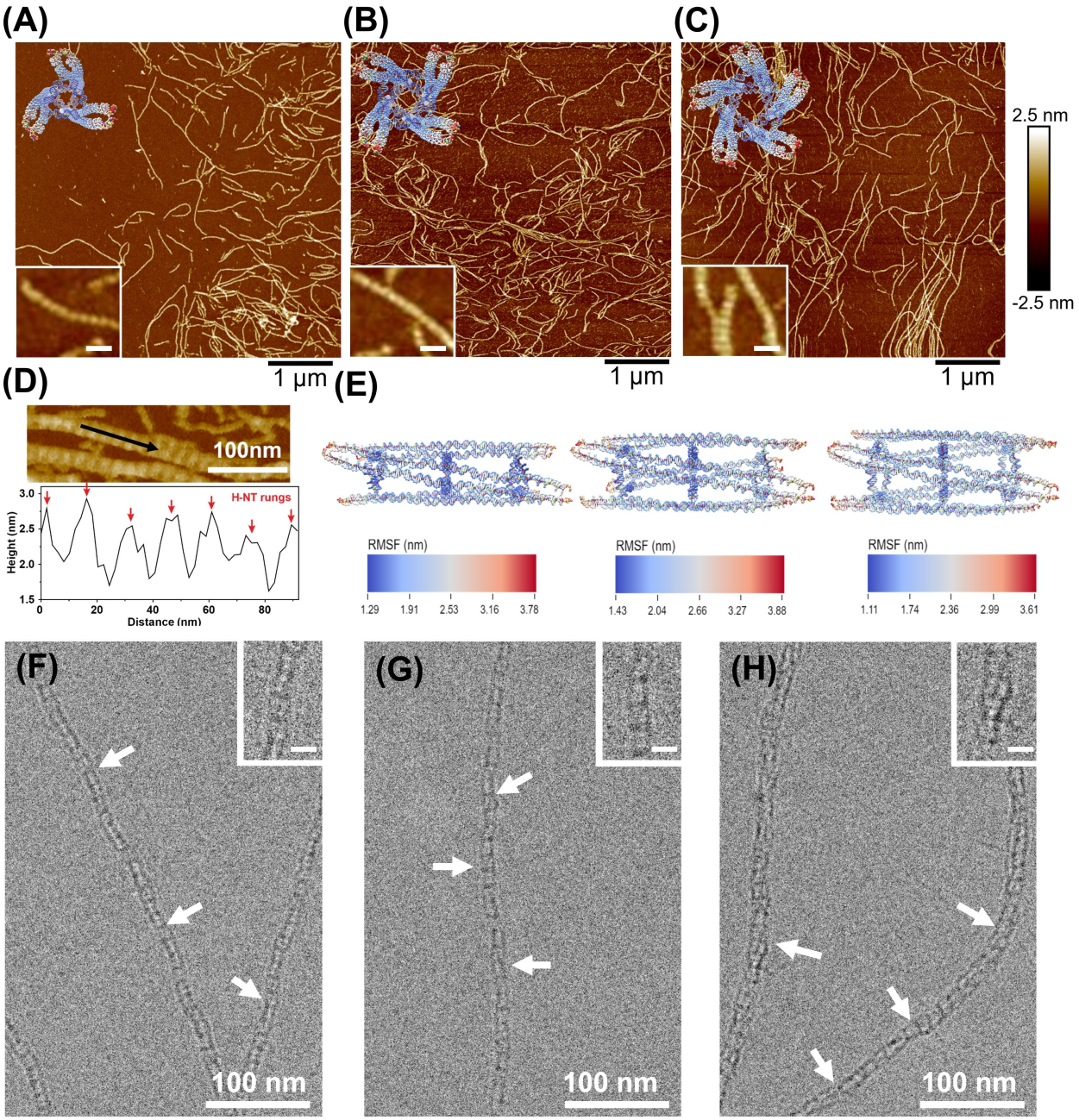

Figure 2. Structures of **H-NT** with various cross-sectional geometries. AFM images of **H-NTs** assembled using self-complementary rung units with (A) triangular, (B) square, and (C) pentagonal cross-sectional geometries. Scale bars of zoomed insets are 50 nm. (D) Zoomed-in image of (B) and the structure height profile along the **H-NT** axis (arrow). (E) MD simulation mean structures of triangular, square, and pentagonal **H-NT** rung trimers. Cryo-EM images of **H-NT** with (F) triangular, (G) square, and (H) pentagonal cross-sections. Scale bars of insets are 10 nm. White arrows indicate areas with an angular twist.

slight right-handed global twist of rungs in the full **H-NT** structure (Figure 1F). We attribute this to the intrinsic bending and twisting of the DX-tile-like structure due to the non-integer crossover design (Figure S3B). Interestingly, this global twist is easily tunable by altering the crossing point of the h-strand (red sequence) in the h-motif structure (Figure 4). We examined the global twist of the pentagonal **H-NTs** by altering the crossing sites within the rung unit and conducting MD simulations and cryo-EM measurements. The rotational angle between the first and third rung in the mean configuration of the MD simulation represents the twist angle of each **H-NT** consisting of three rung units. Here, the twist angle was only measured between the first and third rung. In an extended nanotube assembly, the nanotube's twist will build up with each addition of a rung unit. Experimentally, cryo-EM images clearly showed a global twist for **H-NT**, particularly for square and pentagonal nanotubes (white arrows in Figure 2G,H) and to a lower

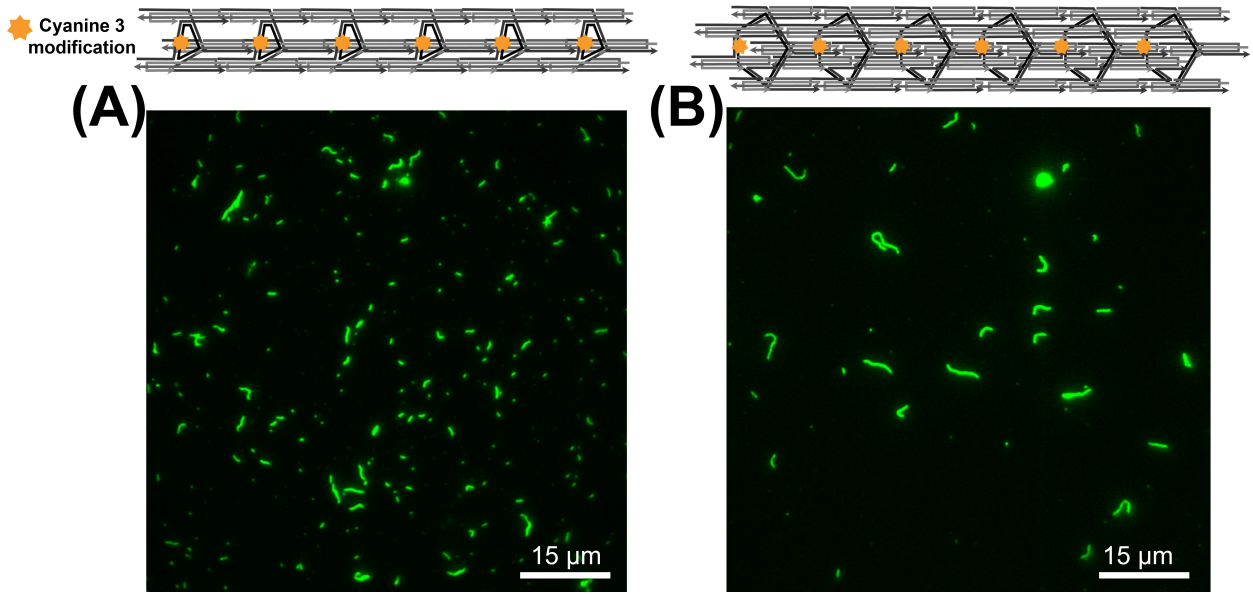

Figure 3. TIRF images of Cy3 **H-NTs**. Typical TIRFM images of Cy3 labeled **H-NTs** having (A) triangular and (B) pentagonal cross-sectional geometries.

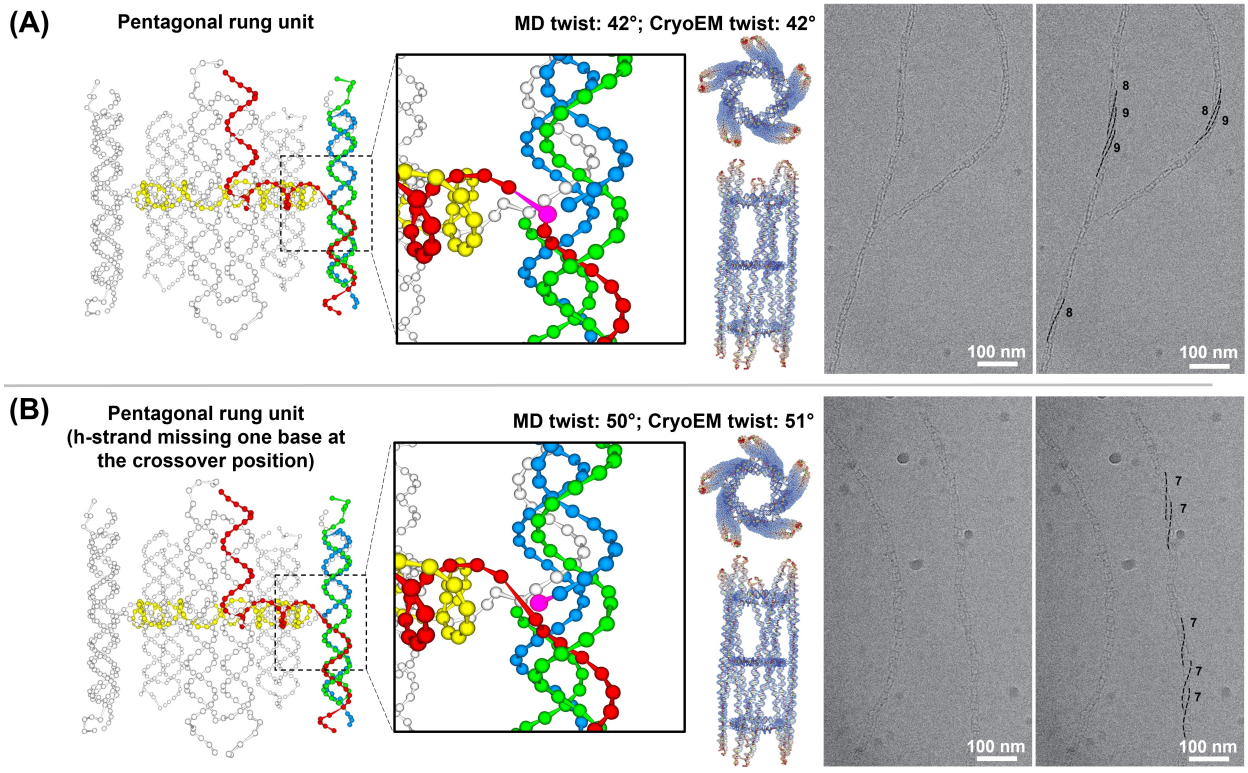

Figure 4. Tuning the global twist of pentagonal **H-NT**. MD simulations and cryoEM images of **H-NT** with various crossover positions; (A) **H-NT** assembled using h-strand with a crossover position (0). (B) The deletion of one base (highlighted in pink) from the h-strand (red sequence) and its addition to the T2 strand (blue sequence) resulted in a change in the twist angle. Half-helical pitches were counted by tracing the double-duplex arms along the **H-NTs** from one side to the other, as indicated in the cryoEM images.

extent for the triangular nanotubes (white arrows in Figure 2F).

The tunable global twist is illustrated in Figure 4, where a global twist of 42° is observed for the original pentagonal **H-NT** (Figure 4A) and a global twist of 51° when the crossover position of the h-strand changes by deleting one nucleotide (pink) from the h-strand (red sequence) and adding it to the T2 strand (blue sequence) (Figure 4B). Of

note, the simulated global twists are highly consistent with the experimental data calculated from the cryo-EM images. This significant change in structural chirality has considerable potential for dynamic chiroptical applications. For instance, metal nanoparticles can be joined to the **H-NT** scaffold, where their chiral plasmonic characteristics would be regulated by the global helicity of the nanotube, all using 4 strands to construct the nanotube.

Interestingly, we discovered a simple method to tune the length of these nanotubes. We introduced an overhang at the rung ends; by adding DNA invader strands that are partially complementary to this overhang, both size and dispersity could be modified. First, a 10-adenine sequence overhang was introduced to elongate the 3′ sticky-ends of the T2 arm strand (blue strand, Figure 1A), yielding **H-NT-10A** (Figure 5A, dark blue). Upon incubation at room temperature (20 °C) with a full-length invading strand, which is complementary to the 5-nucleotide sticky end of the T2 strand and the 10-adenine overhang, the **H-NT** disassembled into individual rungs via strand displacement (Figure 5B). Similar results were observed when the fully complementary invading strand was added during the thermal annealing process (Figure S35).

We found that with shorter invading strands that are complementary to the 5-nucleotide sticky end of the T2 strand and only to a part of the 10-adenine overhang (e.g., a 10-nt strand complementary only to 5 adenines and the 5-nucleotide sticky end), the nanotube did not disassemble into its component rungs. Instead, nanotubes shorter than **H-NT-10A** and with a relatively narrower length distribution were obtained (Figure 5C and Table 1). Moreover, the length of the **H-NT** decreased with increasingly longer

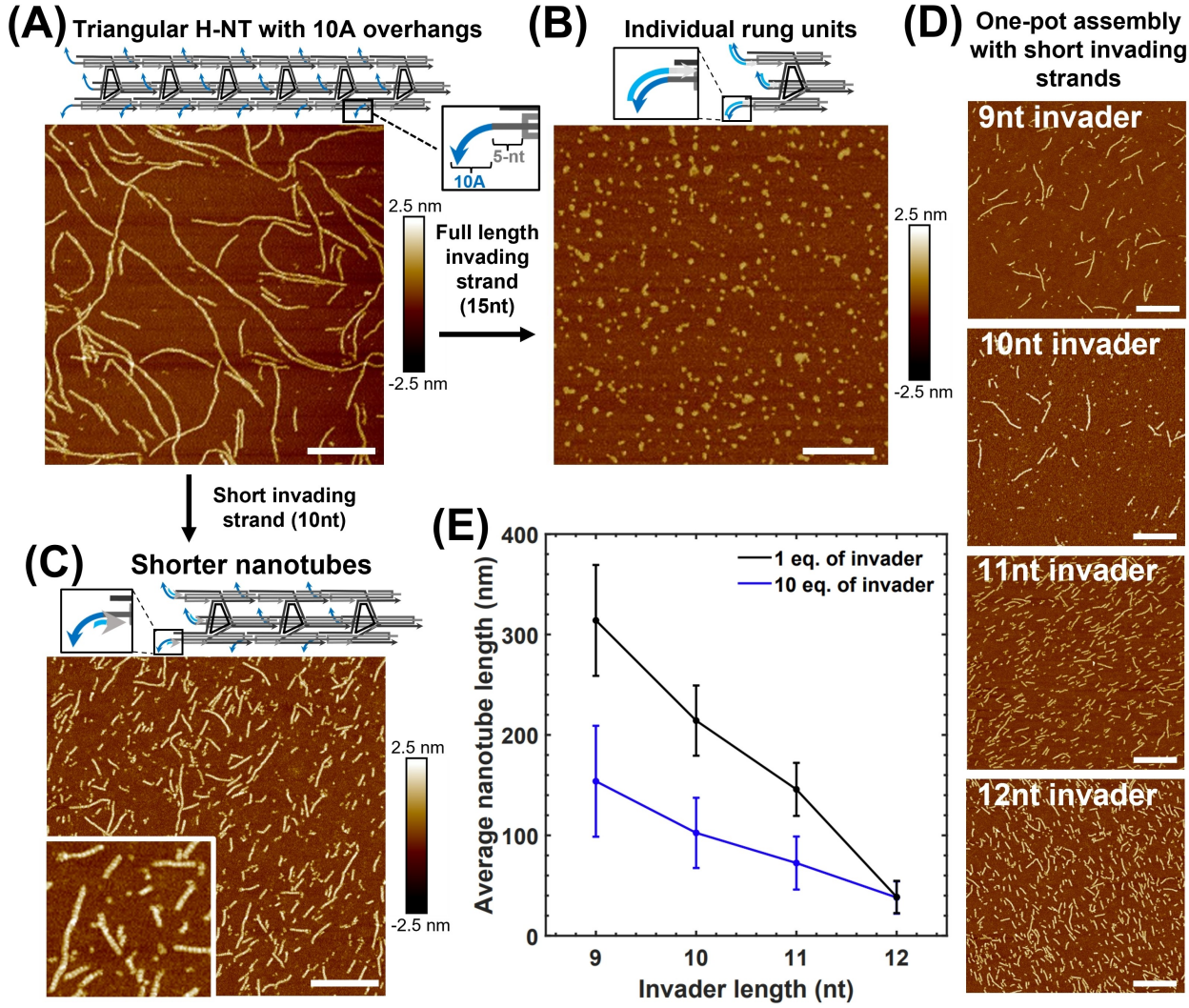

Figure 5. **H-NT** length control with sticky end overhangs and invading strands. (A) AFM images depicting the assembly of **H-NT** with 10-adenine overhang extensions (**H-NT-10A**) at the 3′ end of the T2 strand into long nanotubes. (B) **H-NT-10A** disassembles into individual rungs after incubating with full-length (15-nt) invading strands. (C) **H-NT-10A** disassembles into short **H-NTs** after incubating with a short invading strand (10-nt). (D) **H-NT-10A** of various lengths assembled by annealing the **H-NT** strands with one equivalent of invading strands of different lengths. (E) The change of **H-NT-10A** length is controlled by a short invading strand (1 or 10 equivalents per sticky end, N = 200 for each data set). Scale bars are equal to 400 nm.

Table 1: Average contour lengths of triangular **H-NT-10A** formed in the presence of 1 or 10 equivalents of invading strands with varied complementarity to the **H-NT-10A** overhang. N = 200 for all samples.

H-NT-10A	9-nt invader	10-nt invader	11-nt invader	12-nt invader
1 equivalent of invading strand	314 ± 132 nm	214 ± 93 nm	145 ± 55 nm	39 ± 14 nm
10 equivalents of invading strand	153 ± 55 nm	102 ± 34 nm	72 ± 26 nm	38 ± 16 nm

invader strands (Figure 5D, E). We also noticed that the stoichiometry of the invading strand affects the final **H-NT** length (Figure 5E and Figure S37), with higher equivalents resulting in shorter nanotubes. (e.g., ca. 214 nm to 102 nm with ten times more invader strands).

These results indicate that invading strand binding competes with rung stacking. The fact that nanotubes shorten but do not fully dissociate into individual rungs with partially complementary invaders may point to regions of weaker binding within the nanotubes that these strands can displace. As the length or concentration of the invading strand increases, the binding to the 10-adenine overhang becomes more favorable or occurs more rapidly, forming shorter tubes. Similar results were observed when the partially complementary invading strand was added during the thermal annealing process or after **H-NT-10A** formation and overnight incubation at room temperature (Figure S38). Hence, this strategy provides a simple method to modulate the **H-NT** length, which, to the best of our knowledge, has not been demonstrated for extended DNA structures. The nanotube sizes obtained (40 nm to 300 nm) are in a favorable range for in vivo applications.

Due to the self-complementary nature of the **H-NT** rung design, the assembly of individual rungs into NTs proceeds during the same annealing process as the formation of individual rungs. To gain better structural control and to incorporate site-specific functionality, we replaced the self-complementary sticky-ends with two mutually complementary sticky-ends, residing on two separate rungs (rungs "A" and "B"). Rungs "A" and "B" of different geometries can be formed separately (Figure 6A,B) and can then assemble together into an **H-NT** with alternating rungs (Figure 6C). The formation of well-defined and extended nanotube structures required annealing the rung mixture from 55 to 20 °C (Figure 6E), temperatures that are lower than the rung melting temperature; direct mixing of the two rungs at room temperature resulted in random aggregation (Figure 6D). We hypothesize that the large number of sticky ends per rung increases binding affinity and slows down unbinding, which is necessary for the error correction of malformed products.

To further validate the formation of **H-NT** with alternating rungs, Cy3- and Cy5-modified rungs "A" and "B" were assembled. Native PAGE revealed the proper formation of Cy-labeled rung units (Figure S24). AFM confirmed the formation of well-defined and extended nanotube structures (**H-NT$_{Acy3Bcy5}$**, Figure S25A). TIRF revealed a uniform distribution of both dyes along the nanotube, and the overlap between the two channels indicates that Cy3 and Cy5 are co-localized, indicating that they are in proximity (Figure S25B–D).

Considering their potential applications in synthetic biology, e.g., as cytoskeleton mimics, it would be desirable to assemble the nanotubes at a physiologically relevant temperature, rather than with thermal annealing. The aggregates obtained at room temperature (see above) likely result from the presence of multiple sticky ends per rung. Thus, we hypothesized that temporarily inactivating these sticky ends and controlling their reactivation rate may result in the assembly of the nanotubes at a physiologically relevant temperature. To slowly reveal the sticky ends of the rung units and thus modulate the dynamic assembly of the **H-NTs**, we employed complementary RNA invading strands combined with the enzyme RNase H, an endoribonuclease that specifically hydrolyzes the RNA strand in an RNA/DNA heteroduplex. We first added a fully complementary RNA invading strand (4 equiv.) to the nanotubes with 10 A overhangs, resulting in the complete disassembly of **H-NT-10A** into individual rungs (Figure S46A). The RNA/DNA heteroduplex resulting from strand displacement is a substrate of the RNase H. Enzymatic degradation of the RNA invading strand can be used to reactivate the sticky ends in the individual rung units, which thus re-assemble into **H-NT-10A**. Depending on the amount of RNase H, it is possible to modulate the kinetics of RNA degradation and thus control the reactivation kinetics of the sticky ends.[60] We first confirmed the disassembly of individual rungs in the presence of fully complementary invading RNA strands by AFM. We then monitored re-assembly upon incubation with RNase H for 1 week. We first tested higher levels of RNase H (50 U/mL): in this case, the individual rungs tend to aggregate, collapse, or form shorter structures (Figure S45), consistent with the rapid reactivation of their sticky ends. Upon decreasing the amount of RNase H to 10 U/mL, well-defined and elongated nanotube structures were obtained (Figure S46B). These results indicate that at low levels of RNase H, the RNA invading strand is degraded slowly over time, allowing a slow reactivation of the rung's sticky ends and dynamic error correction of the rung stacking, which eventually proceeds towards nanotube formation. On the other hand, adding a larger amount of RNase H rapidly reactivates the sticky ends resulting in random aggregation. This process could be accelerated to 1 day by using the minimum concentration of RNA invader that results in full disassembly of **H-NT-10A** into individual rungs (1.75 equiv.) while maintaining the RNase H concentration constant (10 U/mL) (Figure 7). Since RNase H is present in cells, a possible future application is the in situ RNase H-mediated polymerization of the nanotubes inside cells.

Having explored the assembly of **H-NT$_{AB}$**, where all rung arms have the same sequence, we next explored the assembly of **H-NT$_{AB}$** rung units with arms of different sequences to further increase nanotube addressability. Native PAGE indicated the formation of distinct bands corresponding to the asymmetric rungs "A_{asym}" and "B_{asym}"

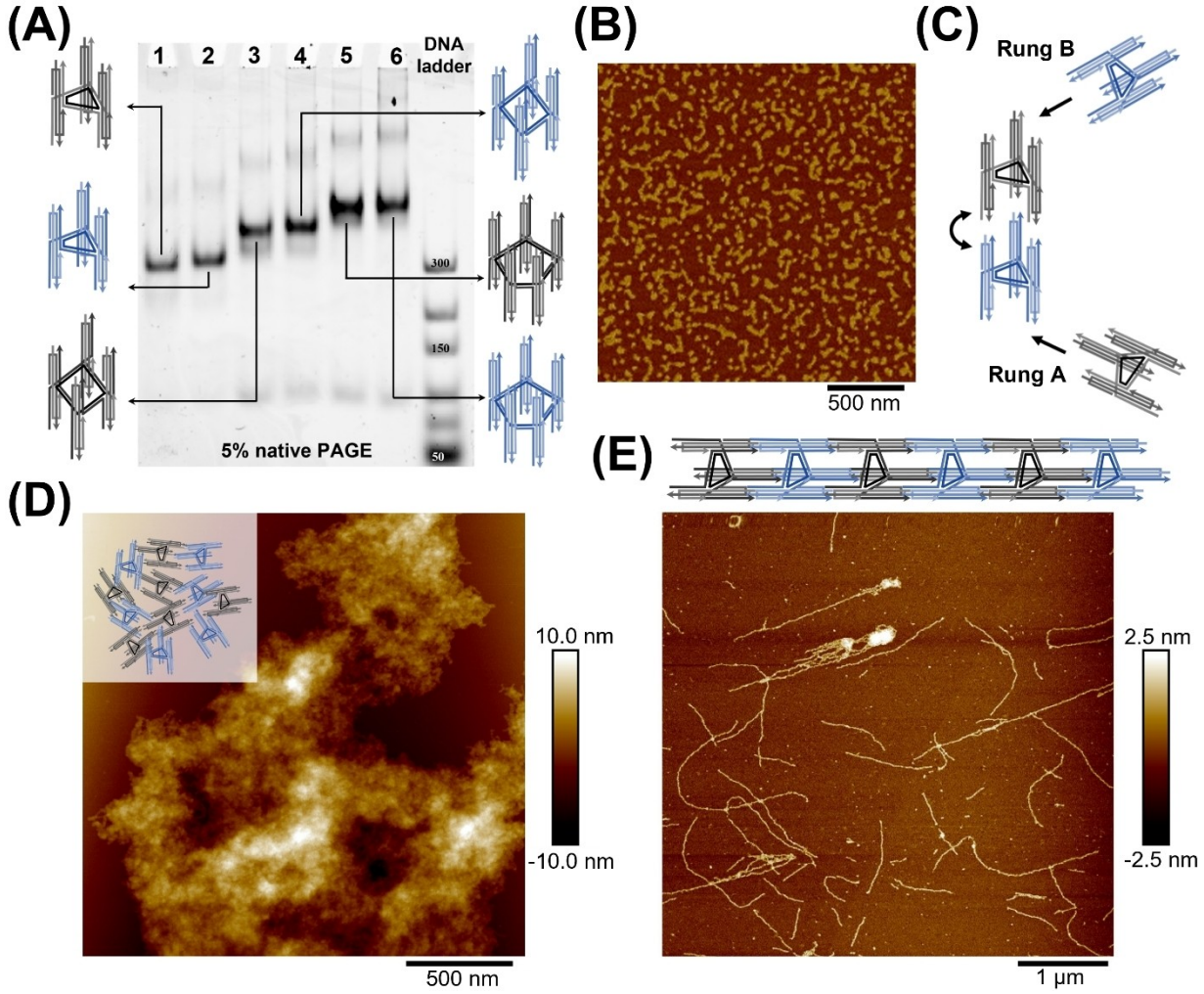

Figure 6. The assembly of **H-NT$_{AB}$** with alternating rungs. (A) 5% native PAGE analysis of rung "A" (black) and rung "B" (blue) monomers with triangular (lanes 1 and 2), square (lanes 3 and 4), and pentagonal (lanes 5 and 6) geometry. (B) AFM image of rung "A" monomers. (C) The design of rung "A" and rung "B" assembled into alternating structures that lead to aggregation. (D) AFM image of random aggregation when mixing rungs "A" and "B" at room temperature. (E) AFM image of **H-NT$_{AB}$** with alternating triangular rungs formed by annealing rung "A" and rung "B" mixture from 55 to 20°C. Full-size gel for Figure 6A is shown at Figure S50.

(Figure S40). Unlike the symmetrical **H-NT** assembled with alternating rung units that resulted in random aggregation, direct mixing of the two asymmetric rungs at room temperature resulted in short nanotubes. Annealing the mixture, in turn, generated well-defined and extended structures (Figure 8). When all the sticky ends are different, the possibility of rung misalignment upon assembly decreases, thus decreasing aggregate formation upon room temperature assembly. The formation of **H-NTs** using alternating rung units also offers up to ten additional uniquely addressable sites within a single rung unit.

Conclusion

In summary, we described a minimalist design of robust wireframe nanotubes with just four DNA sequences. Despite their simple design, the **H-NTs** are highly modular and offer programmable cross-sectional geometry, cavity size, chirality, and length. We produced micrometer-long DNA nanotubes with various cross-sectional patterns, including triangular, square, and pentagonal geometries. This was achieved by introducing the h-motif, a new component that allows the assembly of repeating DX-tile-like double DNA-duplex edges onto a circularly folded strand to form a rigid rung building block. By altering the crossover sites in the h-motif, we demonstrated control over the chirality of our nanotubes. During assembly, partially complementary invading strands can control the nanotube's length. **H-NTs** can be symmetrical and formed with self-complementary rung units, or they can be built with alternating rung units that offer additional unique sites along the nanotube. Asymmetric rungs with different sequences at each arm can further increase the site-specific functionalization ability.

Our nanotubes are supramolecular polymers, where the monomers are rung units with multiple sticky ends. We used

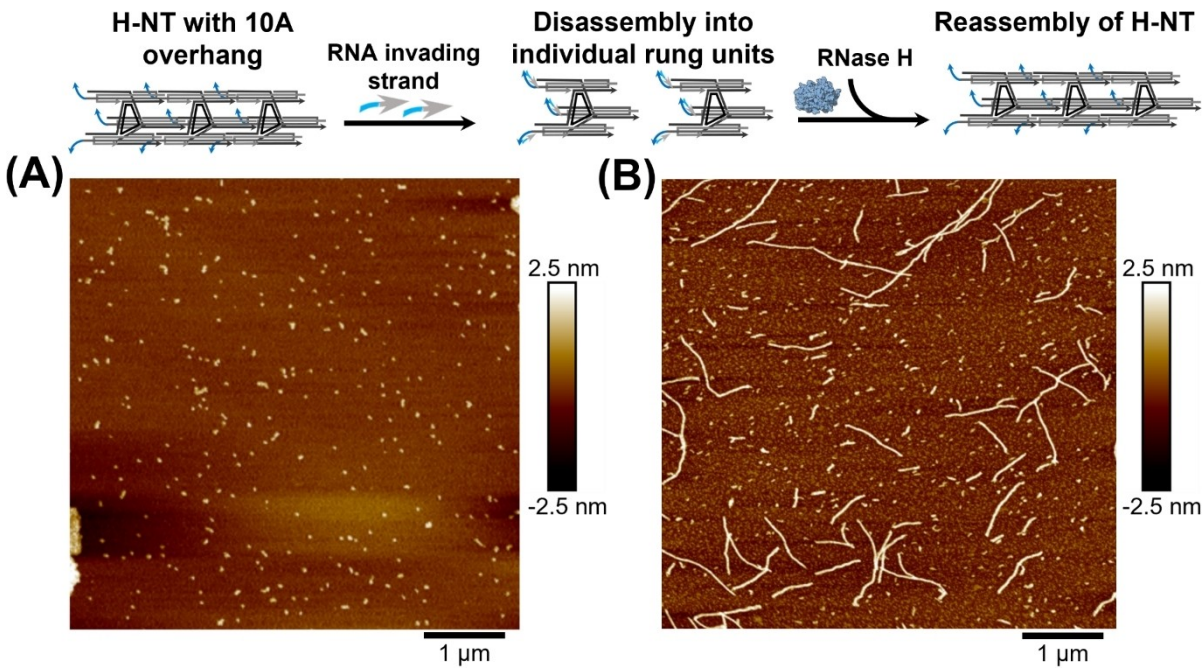

Figure 7. Dynamic control of triangular **H-NT** self-assembly. Reaction Scheme and AFM images of (A) RNA invasion of **H-NT-10A** and (B) **H-NT-10A** reassembly upon addition of 10 U/mL of RNase H and incubation at 30 °C for 1 day.

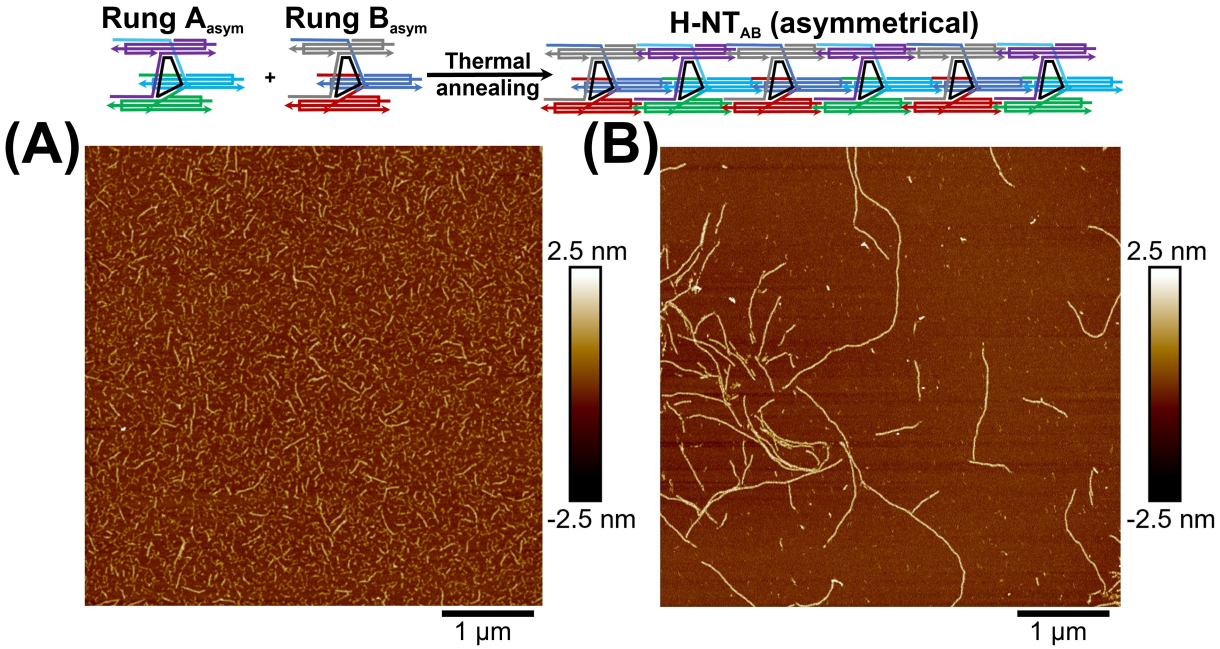

Figure 8. AFM images of asymmetrical **H-NT$_{AB}$** with "h" motifs having unique sequence domains resulting from the mixture of 1 equivalent of rung "A$_{asym}$" with 1 equivalent of rung "B$_{asym}$" and incubated at (A) room temperature or (B) annealed from 55 to 20 °C at a cooling rate of 30 minutes per degree.

a dynamic enzymatic system (RNA invaders and RNase H) to correctly assemble them at a physiologically relevant temperature: this works by slowly releasing and reactivating their sticky ends, allowing for error correction. These DNA-minimal nanotube architectures will serve as easily synthesized, DNA-economical templates for accurate patterning of nanoparticles, proteins, or other ligands, or for in situ, enzymatically triggered growth. In addition, their stability in low-magnesium buffer makes them ideal candidates for use as molecular scaffolds in biomedical and drug-delivery applications.

Author Contributions

X. L. designed the **H-NT**, performed all MD simulations, performed some of the experiments, and co-wrote the manuscript. D. S. helped in the design of the **H-NT**, performed most of the experiments and co-wrote the manuscript. T. Y. and A. G. collected and analyzed cryo-EM images. S. G., N. B. and A. P. designed and performed the RNA invading experiment. K. M. performed some of the DNA-invading experiments. P. I. and G. C. collected and analyzed the fluorescence images. T. D. collected AFM images of some of the asymmetrical nanotubes. H. F. S. designed the project, guided the interpretation of data and results discussion, and co-wrote the paper.

Acknowledgements

We thank the Natural Sciences and Engineering Research Council of Canada (NSERC), the Canada Research Chairs Program, and the Canada Council for the Arts (Killam fellowship) for financial support. H. F. S. is a Cottrell Scholar of the Research Corporation. We thank Marie Skłodowska-Curie Actions (MSCA) for funding S. G. and N. B. visit to McGill university. K. M. thanks Prof. Mitsuhiko Shionoya for supporting his internship at McGill University.

Conflict of Interest

The authors declare no conflict of interest.

Data Availability Statement

The data that support the findings of this study are available from the corresponding author upon reasonable request.

Keywords: Biocompatible DNA Structures · Controlled Chirality · DNA Nanotubes · Dynamic Self-Assembly · Tunable Geometry

[1] X. Liu, Y. Zhao, P. Liu, L. Wang, J. Lin, C. Fan, *Angew. Chem. Int. Ed.* **2019**, *58*, 8996–9011.
[2] N. C. Seeman, H. F. Sleiman, *Nat. Rev. Mater.* **2017**, *3*, 17068.
[3] A. Lacroix, H. F. Sleiman, *ACS Nano* **2021**, *15*, 3631–3645.
[4] O. I. Wilner, R. Orbach, A. Henning, C. Teller, O. Yehezkeli, M. Mertig, D. Harries, I. Willner, *Nat. Commun.* **2011**, *2*, 540.
[5] F. A. Aldaye, P. K. Lo, P. Karam, C. K. McLaughlin, G. Cosa, H. F. Sleiman, *Nat. Nanotechnol.* **2009**, *4*, 349–352.
[6] P. K. Lo, P. Karam, F. A. Aldaye, C. K. McLaughlin, G. D. Hamblin, G. Cosa, H. F. Sleiman, *Nat. Chem.* **2010**, *2*, 319–328.
[7] X. Shen, Q. Jiang, J. Wang, L. Dai, G. Zou, Z.-G. Wang, W.-Q. Chen, W. Jiang, B. Ding, *Chem. Commun.* **2012**, *48*, 11301–11303.
[8] S. Ko, H. Liu, Y. Chen, C. Mao, *Biomacromolecules* **2008**, *9*, 3039–3043.
[9] S. Zhou, X. Cai, Y. Zhang, Q. Chen, X. Yang, K. Wang, L. Jian, J. Liu, *J. Mater. Chem. B* **2022**, *10*, 8322–8329.
[10] P. Zhan, K. Jahnke, N. Liu, K. Göpfrich, *Nat. Chem.* **2022**, *14*, 958–963.
[11] J. R. Burns, A. Seifert, N. Fertig, S. Howorka, *Nat. Nanotechnol.* **2016**, *11*, 152–156.
[12] J. R. Burns, E. Stulz, S. Howorka, *Nano Lett.* **2013**, *13*, 2351–2356.
[13] P. Stömmer, H. Kiefer, E. Kopperger, M. N. Honemann, M. Kube, F. C. Simmel, R. R. Netz, H. Dietz, *Nat. Commun.* **2021**, *12*, 4393.
[14] R. Jungmann, M. S. Avendaño, J. B. Woehrstein, M. Dai, W. M. Shih, P. Yin, *Nat. Methods* **2014**, *11*, 313–318.
[15] A. Kuzyk, R. Schreiber, Z. Fan, G. Pardatscher, E.-M. Roller, A. Högele, F. C. Simmel, A. O. Govorov, T. Liedl, *Nature* **2012**, *483*, 311–314.
[16] K. Zhou, Y. Ke, Q. Wang, *J. Am. Chem. Soc.* **2018**, *140*, 8074–8077.
[17] J. Sharma, R. Chhabra, A. Cheng, J. Brownell, Y. Liu, H. Yan, *Science* **2009**, *323*, 112–116.
[18] A. M. Maier, W. Bae, D. Schiffels, J. F. Emmerig, M. Schiff, T. Liedl, *ACS Nano* **2017**, *11*, 1301–1306.
[19] A. Rangnekar, K. V. Gothelf, T. H. LaBean, *Nanotechnology* **2011**, *22*, 235601.
[20] P. W. Rothemund, A. Ekani-Nkodo, N. Papadakis, A. Kumar, D. K. Fygenson, E. Winfree, *J. Am. Chem. Soc.* **2004**, *126*, 16344–16352.
[21] X. Shi, X. Wu, T. Song, X. Li, *Nanoscale* **2016**, *8*, 14785–14792.
[22] A. Kuzuya, R. Wang, R. Sha, N. C. Seeman, *Nano Lett.* **2007**, *7*, 1757–1763.
[23] J. C. Mitchell, J. R. Harris, J. Malo, J. Bath, A. J. Turberfield, *J. Am. Chem. Soc.* **2004**, *126*, 16342–16343.
[24] Y. Zhang, X. Chen, G. Kang, R. Peng, V. Pan, R. Sundaresan, P. Wang, Y. Ke, *J. Am. Chem. Soc.* **2019**, *141*, 19529–19532.
[25] D. Y. Zhang, R. F. Hariadi, H. M. Choi, E. Winfree, *Nat. Commun.* **2013**, *4*, 1965.
[26] L. N. Green, H. K. Subramanian, V. Mardanlou, J. Kim, R. F. Hariadi, E. Franco, *Nat. Chem.* **2019**, *11*, 510–520.
[27] L. N. Green, A. Amodio, H. K. Subramanian, F. Ricci, E. Franco, *Nano Lett.* **2017**, *17*, 7283–7288.
[28] E. Del Grosso, L. J. Prins, F. Ricci, *Angew. Chem. Int. Ed.* **2020**, *59*, 13238–13245.
[29] S. Agarwal, E. Franco, *J. Am. Chem. Soc.* **2019**, *141*, 7831–7841.
[30] N. Farag, G. Ercolani, E. Del Grosso, F. Ricci, *Angew. Chem. Int. Ed.* **2022**, *61*, e202208367.
[31] J. Le, D. Osmanovic, M. A. Klocke, E. Franco, *ACS Nano* **2022**. *16*, 16372–16384.
[32] S. Agarwal, M. A. Klocke, P. E. Pungchai, E. Franco, *Nat. Commun.* **2021**, *12*, 3557.
[33] P. Yin, R. F. Hariadi, S. Sahu, H. M. Choi, S. H. Park, T. H. LaBean, J. H. Reif, *Science* **2008**, *321*, 824–826.
[34] P. W. Rothemund, *Nature* **2006**, *440*, 297–302.
[35] F. Benn, N. E. Haley, A. E. Lucas, E. Silvester, S. Helmi, R. Schreiber, J. Bath, A. J. Turberfield, *Angew. Chem. Int. Ed.* **2018**, *57*, 7687–7690.
[36] J. F. Berengut, J. C. Berengut, J. P. Doye, D. Prešern, A. Kawamoto, J. Ruan, M. J. Wainwright, L. K. Lee, *Nucleic Acids Res.* **2019**, *47*, 11963–11975.
[37] B. Teshome, S. Facsko, A. Keller, *Nanoscale* **2014**, *6*, 1790–1796.
[38] B. Zhu, J. Guo, L. Zhang, M. Pan, X. Jing, L. Wang, X. Liu, X. Zuo, *ChemBioChem* **2019**, *20*, 1508–1513.
[39] S. Groeer, A. Walther, *Nanoscale* **2020**, *12*, 16995–17004.
[40] J. Hahn, S. F. Wickham, W. M. Shih, S. D. Perrault, *ACS Nano* **2014**, *8*, 8765–8775.

[41] S. Dey, C. Fan, K. V. Gothelf, J. Li, C. Lin, L. Liu, N. Liu, M. A. Nijenhuis, B. Saccà, F. C. Simmel, *Nat. Rev. Methods Primers* **2021**, *1*, 13.
[42] G. D. Hamblin, J. F. Rahbani, H. F. Sleiman, *Nat. Commun.* **2015**, *6*, 7065.
[43] P. K. Lo, F. Altvater, H. F. Sleiman, *J. Am. Chem. Soc.* **2010**, *132*, 10212–10214.
[44] E. Benson, A. Mohammed, J. Gardell, S. Masich, E. Czeizler, P. Orponen, B. Högberg, *Nature* **2015**, *523*, 441–444.
[45] M. Matthies, N. P. Agarwal, T. L. Schmidt, *Nano Lett.* **2016**, *16*, 2108–2113.
[46] W. Ma, Y. Zhan, Y. Zhang, C. Mao, X. Xie, Y. Lin, *Signal Transduction Targeted Ther.* **2021**, *6*, 351.
[47] C. Zhang, M. Su, Y. He, X. Zhao, P.-a. Fang, A. E. Ribbe, W. Jiang, C. Mao, *Proc. Natl. Acad. Sci. USA* **2008**, *105*, 10665–10669.
[48] H. Jun, T. R. Shepherd, K. Zhang, W. P. Bricker, S. Li, W. Chiu, M. Bathe, *ACS Nano* **2019**, *13*, 2083–2093.
[49] A. R. Chandrasekaran, O. Levchenko, *Chem. Mater.* **2016**, *28*, 5569–5581.
[50] H. Jun, X. Wang, M. F. Parsons, W. P. Bricker, T. John, S. Li, S. Jackson, W. Chiu, M. Bathe, *Nucleic Acids Res.* **2021**, *49*, 10265–10274.
[51] D. Saliba, X. Luo, F. J. Rizzuto, H. F. Sleiman, *Nanoscale* **2023**, *15*, 5403–5413.
[52] Y. Tian, T. Wang, W. Liu, H. L. Xin, H. Li, Y. Ke, W. M. Shih, O. Gang, *Nat. Nanotechnol.* **2015**, *10*, 637–644.
[53] Y. He, T. Ye, M. Su, C. Zhang, A. E. Ribbe, W. Jiang, C. Mao, *Nature* **2008**, *452*, 198–201.
[54] K. E. Bujold, A. Lacroix, H. F. Sleiman, *Chem* **2018**, *4*, 495–521.
[55] A. R. Chandrasekaran, *Nat. Chem. Rev.* **2021**, *5*, 225–239.
[56] J. Bohlin, M. Matthies, E. Poppleton, J. Procyk, A. Mallya, H. Yan, P. Šulc, *Nat. Protoc.* **2022**, *17*, 1762–1788.
[57] E. Poppleton, R. Romero, A. Mallya, L. Rovigatti, P. Šulc, *Nucleic Acids Res.* **2021**, *49*, W491-W498.
[58] A. M. Romani, *Arch. Biochem. Biophys.* **2011**, *512*, 1–23.
[59] Y. Gidi, S. Bayram, C. J. Ablenas, A. S. Blum, G. Cosa, *ACS Appl. Mater. Interfaces* **2018**, *10*, 39505–39511.
[60] S. Gentile, E. Del Grosso, P. E. Pungchai, E. Franco, L. J. Prins, F. Ricci, *J. Am. Chem. Soc.* **2021**, *143*, 20296–20301.

Manuscript received: July 11, 2023
Accepted manuscript online: August 23, 2023
Version of record online: September 21, 2023